PHYSICAL REVIEW A **108**, 023515 (2023)

# Optimal generation and systematic analysis of tunable terahertz emissions from single-layer graphene using two-color laser pulses with different durations

Zhong Guan,[1] Zhiming Yin,[1] Jiahao You,[1] Bincheng Wang,[1] Xiaoyong Li,[2] Guo-Li Wang,[3]
Xiao-Xin Zhou,[3] and Cheng Jin[1,4,*]
[1]*Department of Applied Physics, Nanjing University of Science and Technology, Nanjing, Jiangsu 210094, China*
[2]*College of Electrical Engineering, Northwest Minzu University, Lanzhou, Gansu 730030, China*
[3]*College of Physics and Electronic Engineering, Northwest Normal University, Lanzhou, Gansu 730070, China*
[4]*MIIT Key Laboratory of Semiconductor Microstructure and Quantum Sensing,*
*Nanjing University of Science and Technology, Nanjing, Jiangsu 210094, China*

(Received 9 May 2023; accepted 4 August 2023; published 21 August 2023)

We propose that frequency-tunable terahertz (THz) emissions can be efficiently generated from single-layer graphene at normal incidence by optimizing two-color laser pulses. For three different pulse durations, a genetic algorithm (GA) is applied to search for optimal laser parameters, which show quite different characteristics. Resulted THz spectra have different spectral shapes, and their dependence on the relative phase between two colors is dramatically changed with pulse duration. We develop an interference model to explain the THz emissions for three durations, employ a four-wave mixing model to obtain the optimal wavelength of second color for long duration, and use an asymmetry parameter model to describe the THz yields with the relative phase for short duration. We reveal that the dominant mechanism for the THz generation is shifted from the symmetry of laser pulse to the four-wave mixing when the duration of two-color laser is increased. We identify that the shorter duration is better for generating intense THz emission while the longer duration is preferable for selecting the THz frequency. Furthermore, we optimize the two-color laser parameters for maximizing the THz emissions from gapped graphene with the GA. And we also examine the temporal THz waveforms by varying the parameters in the two-color laser pulses.

DOI: 10.1103/PhysRevA.108.023515

## I. INTRODUCTION

Terahertz (THz) emissions have wide applications in science and technology, such as large-scale object imaging [1,2], nonlinear THz spectroscopy [3,4], wireless communications [5], medical diagnosis [6], military aviation [7], and so on. They can be generated coherently through laser-matter interaction by using a variety of media [8–10], and also from the coherent transition radiation from relativistic gas plasma [11]. Due to high atomic densities and stable physical forms, THz emissions from solids have attracted considerable attention. For instance, in 2008, Sagisaka *et al.* [12] observed high-energy protons and THz radiation from laser-irradiated thin-foil targets. In 2011, Hauri *et al.* [13] generated single-cycle THz pulses at a central frequency of 2.1 THz by using organic electrooptic crystals. In 2013, Jeong *et al.* [14] excited the efficient broadband THz waves by implementing the newly made quinolinium crystal. Furthermore, in 2018, Hafez *et al.* [15] generated efficient THz harmonic generation experimentally in single-layer graphene by applying a quasi-monochromatic linearly polarized THz laser pulse through hot Dirac fermions. However, how to optimally increase the conversion efficiency of THz emissions from solids has not been systematically studied so far. On the other hand, to explain the generation mechanism of THz emissions, the transient current model has been widely applied [16]. In this model, a nonvanishing electron current arises during the field ionization in each asymmetric optical cycle, which also allows us to evaluate analytically the structure of emitted THz field by gas photoionization [17,18]. Other models have also been developed, including strong-field approximation [19], four-wave mixing model [20], and full quantum mechanical model by numerically solving time-dependent Schrödinger equation [21–23]. In the four-wave mixing model, the third-order nonlinearity of material is a critical parameter, its inaccuracy could underestimate the THz yields [20,24,25]. The transient current model as one of laser-induced models is difficult to consider the Kerr response and the plasma current oscillations [16,26]. Other promoted approaches based on the laser-induced model in combination with the four-wave mixing model have been applied to discuss the THz emission from the gas plasma [26,27]. However, how to fully understand the THz emissions from solids is still not entirely clear.

To increase the THz yields from solids, one may utilize a scheme of two-color laser pulses. In the past decades, with the advancement of laser technology, it has become possible to manipulate two-color laser pulses. In 2000, by using two-color (fundamental and its second-harmonic fields) laser pulses, Cook and Hochstrasser [28] first reported that the generation of THz waves can be significantly enhanced from laser-induced air plasma. Two-color laser pulses have been

---

[*] Corresponding author: cjin@njust.edu.cn

successfully used to control the electron dynamics in atomic and molecular systems [29–33]. By modifying the ionization, acceleration, and recombination process of electron, the yields of high-order harmonic generation (HHG) can be enhanced, the cutoff energy of HHG can be extended, and THz emissions can be efficiently generated [34–40]. Recently, two-color laser pulses have been applied to control the interband and intraband processes from solids [41] in a number of experimental and theoretical studies. In 2017, Du *et al.* [42] identified that the intensity of second-harmonic plateau can be enhanced in the HHG of ZnO driven by linearly polarized two-color pulses. In 2020, Song *et al.* [43] found that compared to the single-color laser, intensities of high harmonics from ZnO in the plateau region can be enhanced by two to three orders of magnitude when driven by two- or three-color fields. In 2022, Avetissian *et al.* [44] investigated the high-order frequency mixing in graphene and identified that high harmonics originated from the interband transitions are efficiently generated in the case of the orthogonally polarized two-color field. Later on, in a theoretical work, Peng *et al.* [45] uncovered that dephasing is crucial for enhancing asymmetric intraband current when generating THz emissions from one-dimensional MgO with a two-color field in the presence of decoherence effects. And they also concluded that solid-state materials with short dephasing time and long depopulation time would be optimal choice for strong-field THz generation experiments. In the same year, we theoretically demonstrated that THz waves can be efficiently generated from monolayer graphene by using a long-duration two-color laser pulse at normal incidence, which depend on the phase difference between two colors, the laser intensity, and the fundamental wavelength [46]. Although the waveform optimization of the two-color laser has been widely applied for generating the HHG and THz waves from gases [47,48], to the best of our knowledge, it has not been performed for generating THz emissions from solids.

We choose the single-layer graphene as a representative solid material for investigation since it is a two-dimensional (2D) material and exhibits weak screening, high damage threshold, and unique electronic band structures [49–51] and optical properties [52–54]. Thus it results in a large amount of interesting nonlinear optical phenomenon from laser-graphene interaction [12,55,56]. Especially, graphene has some advantages in manipulating THz waves comparing with other 2D materials. In recent years, THz emissions from graphene have been extensively studied in both theory and experiment. For example, by tuning the carrier concentration through either physical or chemical methods, Sensale-Rodriguez *et al.* [57] showed that the interaction between THz waves and graphene can be controllable, which can also be used for designing THz devices. In 2014, Maysonnave *et al.* [58] experimentally used oblique incidence laser pulse with 110 fs to excite the graphene to obtain a coherent THz radiation ranging from 0.1–4 THz via a second-order nonlinear effect. In 2015, Al-Naib *et al.* [59] studied the contributions of interband current and intraband current to THz frequencies band, and found that THz emissions from undoped graphene are sensitive to system parameters and laser parameters. And they also [60] theoretically modeled the third-harmonic generation in doped monolayer graphene at THz frequencies by employing nearest-neighbor tight-binding model and obtained third-harmonic amplitudes as large as 1.6% of the fundamental of the transmitted field. In 2019, Zhu *et al.* [61] gave an experimental evidence of circular photon drag effect in vertically grown graphene by THz emission spectroscopy and suggested that the emitted THz polarization states can be tuned to linear, left-handed, and right-handed elliptical polarizations by changing the helicity of the pump laser. In 2022, Navaeipour *et al.* [62] studied effects of microscopic scattering on THz third-harmonic generation from monolayer graphene and demonstrated that third-harmonic generation is much more sensitive to the nature of the scattering than the linear response. Additionally, few-cycle infrared laser or two-color laser consisting of a fundamental and its second-harmonic fields has been employed to generate low-frequency THz waves from monolayer graphene [63,64]. Considering their potential applications, higher-frequency THz emissions are also desirable. Thus, how to generate THz emissions from single-layer graphene with tunable frequencies is appealing and on demand.

In this work, our goals are twofold. First, we would like to come up with a two-color scheme to efficiently generate THz emissions with tunable frequencies from single-layer graphene. The two-color laser pulses consisting of an 800-nm laser and a near- or midinfrared laser are with different durations and are optimized by using a genetic algorithm (GA). Second, we want to systematically analyze the generation mechanism of THz emissions at different pulse durations of two-color driving lasers. Different models will be applied, such as interference model, four-wave mixing model, and asymmetric parameter model. This paper is organized as follows. In Sec. II, we will give the details of semiconductor Bloch equation of graphene, formula of THz emissions, and two-color optimization procedure with the GA. In Sec. III, we will give the optimized two-color laser parameters, simulate the THz spectra, and analyze the generation mechanism of THz emissions. We will also present the optimal laser parameters from gapped graphene, and will simulate temporal THz waves by varying laser parameters. And we will conclude this work in Sec. IV.

## II. THEORETICAL METHODS

### A. Semiconductor Bloch equation (SBE) of graphene

We employ the time-dependent tight-binding approximation to study the laser-graphene interaction. Under this approximation, band energies near the Dirac points can be precisely calculated. Here we only consider the normal incidence of driving laser, and time-dependent Schrödinger equation can be written as [65]

$$i\hbar\frac{\partial\psi}{\partial t}=\hat{H}(\mathbf{k}+\mathbf{A}(t))\psi, \tag{1}$$

where

$$\hat{H}(t)=\begin{bmatrix}0 & f(\mathbf{k}(t))\\ f^{*}(\mathbf{k}(t)) & 0\end{bmatrix}. \tag{2}$$

One can diagonalize the matrix $\hat{H}(t)$ and yield energy eigenvalues for the valence band $E_v(\mathbf{k}+\mathbf{A}(t)) = -|f(\mathbf{k}+\mathbf{A}(t))|$ and the conduction band $E_c = |f(\mathbf{k}+\mathbf{A}(t))|$, where

$$f(\mathbf{k}(t)) = -\gamma \sum_{\alpha=1}^{3} e^{i(\mathbf{k}+\mathbf{A}(t))\delta_\alpha}, \tag{3}$$

with $\gamma = 3.03$ eV, $\delta_1 = a(0, 1)$, $\delta_{2,3} = \frac{a}{2}(\pm\sqrt{3}, -1)$ are the locations of nearest neighbors separated by distance $a \approx 1.42$Å. Here $\mathbf{A}(t)$ is the vector potential of driving laser. We define the time-dependent wave function $\phi_{\mathbf{k}}(t) = C_{\mathrm{v}}^{\mathbf{k}}(t)\phi_v^{\mathbf{k}} + C_{\mathrm{c}}^{\mathbf{k}}(t)\phi_c^{\mathbf{k}}$, in terms of Bloch basis, $\phi_v^{\mathbf{k}} = (1, 0)^{\mathrm{T}}$and $\phi_c^{\mathbf{k}} = (0, 1)^{\mathrm{T}}$. When using the Bloch basis as a unitary transform, we can obtain the time-dependent Hamilton $\hat{H}_B(t)$ in terms of the Bloch basis [63]. By using $\hat{H}_B(t)\phi_{\mathbf{k}} = i\hbar\frac{\partial\phi_{\mathbf{k}}}{\partial t}$, we get the two-band equations in the following:

$$\begin{aligned} \frac{d}{dt}C_{\mathrm{v}}^{\mathbf{k}} &= i\big[-B_1(t)C_{\mathrm{v}}^{\mathbf{k}} - B_2(t)C_{\mathrm{c}}^{\mathbf{k}}\big] \\ \frac{d}{dt}C_{\mathrm{c}}^{\mathbf{k}} &= i\big[-B_3(t)C_{\mathrm{v}}^{\mathbf{k}} - B_4(t)C_{\mathrm{c}}^{\mathbf{k}}\big], \end{aligned} \tag{4}$$

where $C_v^{\mathbf{k}}$ and $C_c^{\mathbf{k}}$ are coefficients in the valence and conduction bands, respectively. We define $\bar{\rho}_{vv} = (C_v^{\mathbf{k}})^{\dagger}C_v^{\mathbf{k}}$ as the electron population in the valence band, $\bar{\rho}_{cc} = (C_c^{\mathbf{k}})^{\dagger}C_c^{\mathbf{k}}$ as the electron (or hole) population in the conduction band, and $\bar{\rho}_{cv} = (C_v^{\mathbf{k}})^{\dagger}C_c^{\mathbf{k}}$ as the interband polarization. And the coupled semiconductor Bloch equation (SBE) can be obtained as [49],

$$\begin{aligned} \frac{d}{dt}\bar{\rho}_{cv}(t) =& -iB_4^*\bar{\rho}_{cv}(t) + iB_1^*\bar{\rho}_{cv}(t) \\ & - iB_3(1 - f_e - f_h) - \gamma_r\bar{\rho}_{cv}(t), \\ \frac{d}{dt}f_e =& \, 2\,\mathrm{Im}[-B_3^*\bar{\rho}_{cv}(t)] - \gamma_l f_e, \\ \frac{d}{dt}f_h =& \, 2\,\mathrm{Im}[B_2^*\bar{\rho}_{cv}(t)] - \gamma_l f_h, \end{aligned} \tag{5}$$

where $f_e = \bar{\rho}_{cc}$ and $f_h = f_e$ denote the electron and hole populations, respectively, and $\gamma_r$ and $\gamma_l$ are the transverse and longitudinal relaxation constants, respectively [66]. For the most simplified case, near the Dirac cone the SBE can be simplified under the tight-binding approximation. In the electron-hole picture, $\gamma|\sigma(\mathbf{k})| \approx k^2/2m_u + E_g/2$ with the hole mass of $m_\mu$, the band gap energy of $E_g \sim 0$, and $\sigma(\mathbf{k}) = \sum_{\alpha=1}^{3} e^{i\mathbf{k}\delta_\alpha}$, and $\theta_{f(\mathbf{k})} = \theta_{\mathbf{k}}$, where $\theta_{\mathbf{k}}$ defines the directional angle of vector $[k_x, k_y]$ [67].

### B. Formulation of electron current and THz emission

The single electron current can be calculated as

$$j_\kappa(t) = \langle\phi_{\mathbf{k}}(\mathbf{r}, t)|\hat{\mathbf{p}} + \mathbf{A}(t)|\phi_{\mathbf{k}}(\mathbf{r}, t)\rangle, \tag{6}$$

where $\phi_{\mathbf{k}} = C_v^{\mathbf{k}}\phi_v^{\mathbf{k}} + C_v^{\mathbf{k}}\phi_c^{\mathbf{k}}$. $\phi_{\mathbf{k}}$ in Eq. (6) is derived from $\phi_\kappa = U^{\dagger}\psi_{\mathbf{k}}$, here $U$ can be obtained by eigenvector of time-dependent Hamiltonian corresponding to eigenvalue $\epsilon$.

$$U = \frac{1}{\sqrt{2}}\begin{bmatrix} -\mathrm{e}^{\mathrm{i}\theta_{f(\mathbf{k})}} & \mathrm{e}^{\mathrm{i}\theta_{f(\mathbf{k})}} \\ 1 & 1 \end{bmatrix}, \tag{7}$$

where $\theta_{f(\mathbf{k})}$ denotes the phase angle of Eq. (3) at $A(t) = 0$. For a specific $\mathbf{k}$ point, the time-dependent $x$ direction ($y$ direction) current is,

$$\begin{aligned} j_{x(y)}^{\mathbf{k}} &= \langle\phi_{\mathbf{k}}(\mathbf{r}, t)|\hat{p}_{x(y)} + A_{x(y)}(t)|\phi_{\mathbf{k}}(\mathbf{r}, t)\rangle \\ &= 2\big|C_c^{\mathbf{k}}\big|^2 p_{\mathbf{k},x(y)}^{cc} - p_{\mathbf{k},x(y)}^{cc} \\ &\quad + 2Re\big[C_v^{\mathbf{k}}C_c^{\mathbf{k}*}p_{\mathbf{k},x(y)}^{cv}\big] + A_{x(y)}(t), \end{aligned} \tag{8}$$

where $p_{\mathbf{k},x(y)}^{cv}$ and $p_{\mathbf{k},x(y)}^{cc}$(constants) have showed in Ref. [68]. Thus the total current is the addition of the electron current in the first Brillouin region (BZ) as [69]

$$\mathbf{J}(t) = \int_{BZ} j_{x(y)}^{\mathbf{k}} d\mathbf{k}. \tag{9}$$

Here we focus on the transverse current, the THz spectra can be computed via a Fourier transform of the time derivative of the electron current:

$$\mathbf{E}_{\mathrm{THz}}(\omega) \propto \hat{F}\left[\frac{d\mathbf{J}}{dt}\right]. \tag{10}$$

And the THz waveform in the time domain can be obtained by an inverse Fourier transform of the THz emission (including amplitude and phase) for a given spectral range.

### C. Two-color waveform optimization by genetic algorithm

In this work, we consider the single-layer graphene radiated at normal incidence with linearly polarized two-color laser pulses. The electric field $E_p(t)$ of driving laser can be written as

$$\begin{aligned} E_p(t) &= E_{01}(t) + E_{02}(t), \\ E_{01}(t) &= E_1 \cos^4\left(\frac{\omega_1 t}{2n}\right)\cos(\omega_1 t + \phi_1), \\ E_{02}(t) &= E_2 \cos^4\left(\frac{\omega_1 t}{2n}\right)\cos(\omega_2 t + \phi_2). \end{aligned} \tag{11}$$

where $\omega_1$ and $\omega_2$ are the fundamental and the second-color angular frequencies, respectively. $\omega_1$ (or $\lambda_1$) is fixed in the optimization. $E_1$ and $E_2$ are the amplitudes of peak electric field for two wavelength components, respectively. The carrier envelope phase (CEP) of fundamental laser is assumed as $\phi_1 = 0$, and the CEP of second-color field (or the relative phase difference) is $\phi_2$. Pulse durations for two colors are the same. Laser parameters $\{E_1, E_2, \lambda_2, \phi_2\}$ need to be determined in the optimization by using the genetic algorithm (GA) [48].

GA has been widely used in the search and optimization in a multiparameter space, which mimics the process of natural evolution. In GA, each candidate solution (called individual) can mutate and alter, and a population of candidate solutions evolves toward better ones. The optimal process starts with a population of randomly generated individuals, and better individuals are selected from current generation by evaluating the fitness function of each individual, which are then used in the next generation. If a satisfactory fitness level is reached, the evolution process is terminated. In our simulations, the population size is chosen to be 5, the crossover rate is 0.5, and the maximum number of generation is set to be 5000–10000 to guarantee the convergence. Most likely the genetic optimization returns the local extremum rather than the global

TABLE I. Optimized parameters of two-color laser pulses for generating THz emissions at central frequencies 10–40 THz. $|E_1|^2$ and $|E_2|^2$ are laser intensities with the unit of $10^{12}\mathrm{W/cm^2}$, $\alpha$ is the intensity ratio of the fundamental color to the second one. Pulse duration of two-color driving laser is 512 fs.

| Frequency | $\lvert E_1\rvert^2$ | $\lvert E_2\rvert^2$ | $\alpha$ | $\lambda_2$ (nm) | $\phi_2(\pi)$ |
|---|---|---|---|---|---|
| 10 THz | 0.0891 | 0.1084 | 0.822 | 1644.2 | 1.122 |
| 15 THz | 0.0892 | 0.1083 | 0.823 | 1667.1 | 0.570 |
| 20 THz | 0.0894 | 0.1081 | 0.827 | 1690.7 | 0.380 |
| 25 THz | 0.0887 | 0.1088 | 0.815 | 1714.2 | 0.260 |
| 30 THz | 0.0897 | 0.1078 | 0.832 | 1738.8 | 0.213 |
| 35 THz | 0.0888 | 0.1087 | 0.817 | 1764.5 | 0.480 |
| 40 THz | 0.0889 | 0.1086 | 0.818 | 1790.1 | 1.920 |

one [48]. Our goal is to optimize yields of THz emissions at a given frequency $\omega_F$. So the fitness function is taken as

$$F = \int_{\omega_{F1}}^{\omega_{F2}} |\mathbf{E}_{\mathrm{THz}}(\omega)|^2, \tag{12}$$

in which the optimal frequency $\omega_F$ is centered in a small spectral range $[\omega_{F1}, \omega_{F2}]$. For the longest pulse duration of 512 fs, the bandwidth is chosen as 2 THz. This bandwidth is set as 5 THz for other two shorter pulses (106 and 53 fs) because the width of optimal THz spectrum is decreased with the duration of driving laser pulse. Meanwhile, there are some constraints in the optimization. First, a damage fluence threshold of single-layer graphene is below 150 $\mathrm{mJ/cm^2}$. Second, THz yields are always peaked at the optimal frequency. Note that there are four parameters determined by the optimization procedure. Each optimization can be accomplished within a few days with the high-performance computer. However, there is no way to accomplish it by the manual search.

## III. RESULTS AND DISCUSSION

### A. Optimized incommensurate two-color laser pulses for tunable THz emissions

In the simulations, we optimize the two-color laser pulses by choosing three full-width at half-maximum (FWHM) durations, i.e., 512 fs, 106 fs, and 53 fs, respectively. At each optimization, we fix the fundamental wavelength at 800 nm, and preset the central THz frequency. The GA program is applied to search for optimal laser parameters, such as fundamental peak amplitude $E_1$, second-color peak amplitude $E_2$, second-color wavelength $\lambda_2$, and phase difference $\phi_2$. Optimized parameters of two-color laser pulses for tunable central THz frequencies are listed in Tables I–III for three pulse durations, respectively. In Tables I–III, we introduce a parameter $\alpha$ to give the ratio of fundamental intensity to second-color one. Laser parameters at different pulse durations show quite different features. For long pulse duration of 512 fs, $\alpha$ parameter is about stable, the wavelength of second color is gradually increased with the central THz frequency, and the relative phase is changed randomly, see Table I. For short pulse duration of 53 fs, some exceptions occur at 35 THz and 40 THz while the $\alpha$ parameter, the second-color wavelength, and the relative phase are almost not changed by varying the THz frequency, see Table III. Note that the two-color laser waveform resulted from relative phases in the form of $0.25\pi + 0.5n\pi$ with integer value $n$ can be considered as the same since they could produce the same THz yields. We then take a look at parameters for medium pulse duration of 106 fs in Table II. Both the $\alpha$ parameter and the second-color wavelength are increased with the THz frequency while the relative phase is varied within $0.5\pi$. Here the relative phases of 0 and $\pi$ give the same THz results.

TABLE II. Same as Table I, but pulse duration is 106 fs.

| Frequency | $\lvert E_1\rvert^2$ | $\lvert E_2\rvert^2$ | $\alpha$ | $\lambda_2$ (nm) | $\phi_2(\pi)$ |
|---|---|---|---|---|---|
| 10 THz | 0.3892 | 0.5588 | 0.696 | 1601.2 | 0.249 |
| 15 THz | 0.4075 | 0.5405 | 0.753 | 1655.3 | 0.178 |
| 20 THz | 0.4133 | 0.5347 | 0.773 | 1678.2 | 1.002 |
| 25 THz | 0.4166 | 0.5314 | 0.783 | 1705.3 | 0.480 |
| 30 THz | 0.4198 | 0.5282 | 0.795 | 1734.4 | 0.475 |
| 35 THz | 0.4241 | 0.5239 | 0.809 | 1762.5 | 0.010 |
| 40 THz | 0.4264 | 0.5216 | 0.817 | 1789.6 | 0.470 |

We show the simulated THz spectra by using optimized two-color laser pulses with different pulse widths in Figs. 1(a)–1(c), respectively. Besides the THz spectra with central frequencies between 10–40 THz, we also calculate 3-THz spectra for 512 fs, 45-THz spectra for 106 fs, and 80-THz spectra for 53 fs. One can see that there are two distinguished features. First, at each fixed laser duration, the spectral width of THz emission intensity is not changed with the central THz frequency. The FWHM widths are 5.6 THz, 27.8 THz, and 55.4 THz (as labeled in the figures) for laser durations of 512 fs, 106 fs, and 53 fs, respectively. Therefore, one can obtain the second feature that the spectral width is increased with the decrease of laser duration. To further confirm this point, in Fig. 1(d), we plot the Fourier spectra of single-color THz pulses with different durations. The central frequencies and the pulse durations are chosen in the following: 5.7 THz and 512 fs; 26 THz and 106 fs; and 52 THz and 53 fs. The spectral width is decreased with laser pulse duration, and it is about 0.66 times the FWHM width of THz spectra driven by the optimal two-color laser pulses. Note that we expect that THz signals with well tunable central frequencies can be generated by using long-duration (longer than 512 fs) two-color pulses.

The relative phase $\phi_2$ is a key ingredient for composing the waveform of two-color laser pulses. Its dependence on the duration of driving laser has been shown in Tables I–III. Here we provide with additional evidences. First, in the

TABLE III. Same table as Table I except for pulse duration of 53 fs.

| Frequency | $\lvert E_1\rvert^2$ | $\lvert E_2\rvert^2$ | $\alpha$ | $\lambda_2$ (nm) | $\phi_2(\pi)$ |
|---|---|---|---|---|---|
| 10 THz | 0.958 | 1.412 | 0.678 | 1601.3 | 1.249 |
| 15 THz | 0.955 | 1.415 | 0.674 | 1600.3 | 0.249 |
| 20 THz | 0.954 | 1.416 | 0.673 | 1601.3 | 0.249 |
| 25 THz | 0.955 | 1.415 | 0.675 | 1601.6 | 0.249 |
| 30 THz | 0.947 | 1.423 | 0.665 | 1603.3 | 0.749 |
| 35 THz | 0.981 | 1.389 | 0.701 | 1739.5 | 0.210 |
| 40 THz | 1.022 | 1.348 | 0.756 | 1756.2 | 0.350 |

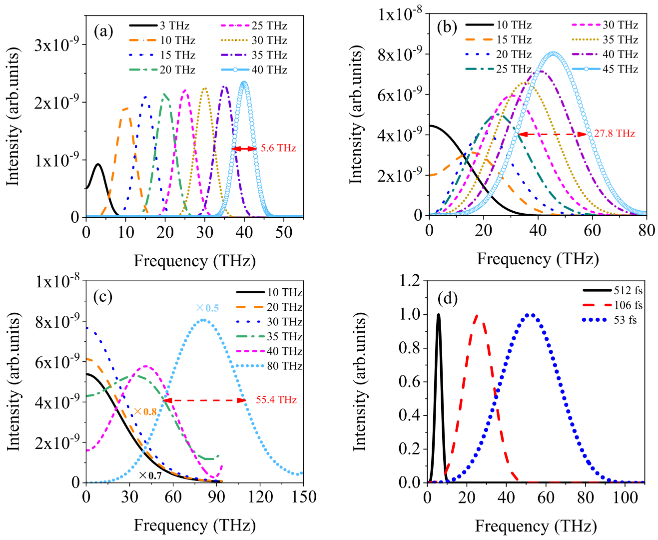

FIG. 1. Simulated THz spectra with tunable central frequencies generated by optimized incommensurate two-color laser pulses for durations of (a) 512 fs, (b) 106 fs, and (c) 53 fs. Laser parameters for simulations are from Tables I–III. FWHM widths of THz spectra are labeled. The Fourier spectra of single-color THz pulses with different durations are shown in (d).

optimization with GA, we can start from different initial random numbers, each number returns a slightly different set of optimal laser parameters (not shown). We have checked that the relative phase is quite stable from different runs for short pulse duration, it is randomly varied for long pulse duration, and its variation can be limited in a small range for medium pulse duration. Second, we take an example of THz spectra at 20 THz by using optimized parameters in Tables I–III, and then the relative phase $\phi_2$ is varied by $2.0\pi$ while the other parameters are maintained. The resulted THz spectra as a function of the relative phase $\phi_2$ are shown in Figs. 2(a), 2(c) and 2(e) for three pulse durations, respectively. For 53 fs, the THz intensity is sensitive to $\phi_2$, and it shows a periodic change with the phase change of $0.5\pi$. For 106 fs, the THz intensity still shows a periodic change with relative phase, but it is less sensitive to $\phi_2$. For 512 fs, the THz intensity doesn't depend on the relative phase at all. The THz spectra for some selected relative phases are plotted in Figs. 2(b), 2(d) and 2(f). These figures also show the quite different dependence of THz intensity on the relative phase by using driving lasers with different durations. We thus can conclude that the subcycle waveform of two-color laser pulses is only significant for optimizing the THz yields when the duration of driving laser is short. This is consistent with what has been found in the optimization of HHG from gases [39,48].

### B. Analysis of tunable THz emissions driven by optimized two-color laser pulses with different durations

To understand the generation mechanism of tunable THz emissions by using different pulse durations of two-color laser, we adopt three models here. The first one is the interference model, which has been simplified from the photoelectron current model. This model is quite general, which can be used to explain the THz emissions for all pulse durations of driving laser. The second one is the four-wave mixing model, which can give a qualitative description of THz emissions driven by a long-duration pulse. The third one is the asymmetric parameter model, which can quantitatively explain the change of THz yields with the relative phase in the two-color field when the laser duration is short.

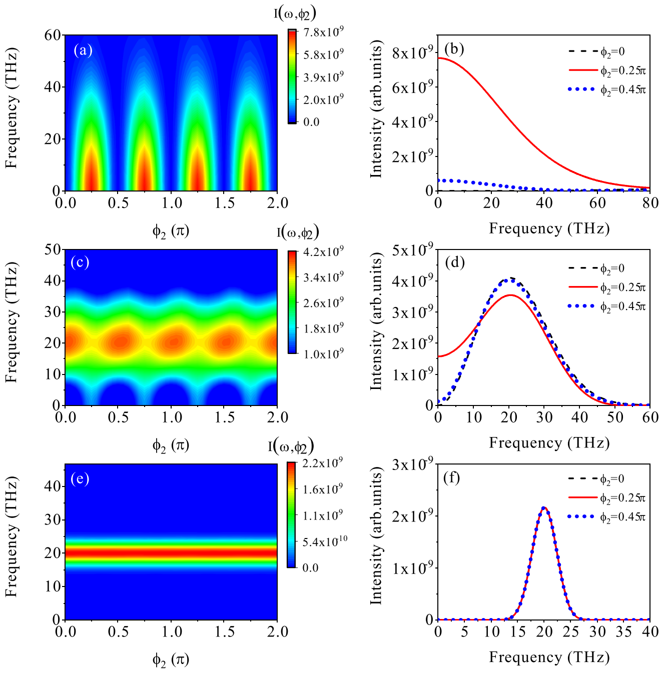

FIG. 2. THz spectra at the central frequency of 20 THz versus relative phase $\phi_2$ for durations of (a) 53 fs, (c) 106 fs, and (e) 512 fs. For simulations, laser parameters except for $\phi_2$ are from Tables I–III. THz spectra at selected $\phi_2$ from (a), (c), and (e) are plotted in (b), (d), and (f), respectively.

#### 1. *Interference model*

The interference model is modified from the photoelectron current model [48], in which the intercycle interference of intraband current plays a major role in the THz emission. In this model, the intraband current can be calculated as [41],

$$\mathbf{j}_{\text{Intra}}(t) = \{\rho_{cc}(t)\mathbf{v}_c[\mathbf{k}(t)] + \rho_{vv}(t)\mathbf{v}_v[\mathbf{k}(t)]\},$$
$$\mathbf{J}_{\text{Intra}}(t) = \int_{BZ} \mathbf{j}_{\text{Intra}}(t)d\mathbf{k}, \tag{13}$$

where $\mathbf{v}_c$ and $\mathbf{v}_v$ are velocities of conduction and valence bands, respectively, $\rho_{cc}$ is the electron population of conduction band, and $\rho_{vv}$ is the same quantity for the valence band. In the nearest-neighbor tight-binding model, $\mathbf{v}_c = -\mathbf{v}_v$, we can simplify the formula as

$$\mathbf{j}_{\text{Intra}}(t) = [\rho_{cc}(t) - \rho_{vv}(t)]\mathbf{v}_c[\mathbf{k}(t)]. \tag{14}$$

At each $\mathbf{k}$, we define $n^{\mathbf{k}}(t) = \rho_{cc}(t) - \rho_{vv}(t)$. Here $n^{\mathbf{k}}(t)$ is related to Landau-Zener tunneling formula while $\mathbf{v}_c[\mathbf{k}(t)]$ is determined by energy band of single-layer graphene and driving laser. The THz spectra can be calculated through a Fourier transform of the time derivative of the electron current, which

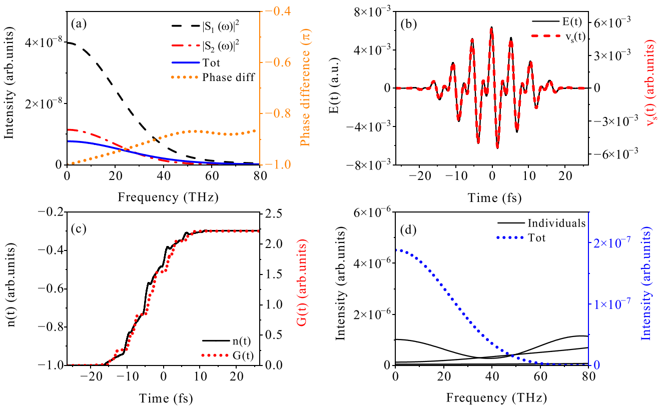

FIG. 3. (a) Intensities of $|S_1(\omega)|^2$ (dashed black line), $|S_2(\omega)|^2$ (dash-dotted red line), and $|S_1(\omega)+S_2(\omega)|^2$ (total, short-dotted blue line), and phase difference between $S_1(\omega)$ and $S_2(\omega)$ (dotted orange line). (b) Comparison of two-color electric field $E(t)$ (solid black line) and electron acceleration in energy band $v_s(t)$ (short-dashed red line) as a function of time. (c) Comparison of population difference $n(t)$ (solid black line) and function $G(t)$ (short-dotted red line) with time. (d) THz emissions from different time intervals in the two-color laser pulse (solid black lines) and THz emissions by coherently adding contributions from all time intervals (short-dotted blue line). This figure is used to demonstrate the interference model. For simulating THz emissions in (d), $E(t)$ and $G(t)$ are used to replace $v_s(t)$ and $n(t)$, respectively. The duration of driving two-color laser pulse is 53 fs.

is written as

$$\frac{d\mathbf{j}_{\text{Intra}}(t)}{dt} = [\rho_{cc}(t)-\rho_{vv}(t)]\frac{d\mathbf{v}_c[\mathbf{k}(t)]}{dt} + \frac{d[\rho_{cc}(t)-\rho_{vv}(t)]}{dt}\mathbf{v}_c[\mathbf{k}(t)]. \tag{15}$$

We first analyze the THz emissions by defining

$$S_1(t) = \int_{BZ}[\rho_{cc}(t)-\rho_{vv}(t)]\frac{d\mathbf{v}_c[\mathbf{k}(t)]}{dt}d\mathbf{k},$$
$$S_2(t) = \int_{BZ}\frac{d[\rho_{cc}(t)-\rho_{vv}(t)]}{dt}\mathbf{v}_c[\mathbf{k}(t)]d\mathbf{k}. \tag{16}$$

We take THz emissions at 20 THz for example. We apply the optimized two-color laser parameters and calculate $S_1(t)$ and $S_2(t)$ for three laser durations. We then obtain their Fourier transform $S_1(\omega)$ and $S_2(\omega)$. Results of $|S_1(\omega)|^2$, $|S_2(\omega)|^2$, and $|S_1(\omega)+S_2(\omega)|^2$ (total) are plotted in Figs. 3(a), 4(a), and 5(a). Meanwhile, phase differences between $S_1(\omega)$ and $S_2(\omega)$ are also plotted in these figures. One can identify two features. First, $|S_1(\omega)|^2$ is dominant in the THz emission regardless of laser duration. Second, the phase difference changes dramatically by varying laser duration. At 53 fs, the phase difference is close to $-\pi$ near 20 THz, corresponding to destructive interference between $S_1(\omega)$ and $S_2(\omega)$, see Fig. 3(a). In Fig. 5(a), the phase difference becomes zero near 20 THz, meaning the constructive interference occurs for 512 fs. For medium duration of 106 fs, the phase difference is mostly distributed between 0 and $-\pi$, see Fig. 4(a). Thus, the interference effect between $S_1(\omega)$ and $S_2(\omega)$ is changed with laser duration. Meanwhile, one can see that $|S_1(\omega)|^2$ always prevails over $|S_2(\omega)|^2$, meaning that the coupling of the electron acceleration and the electron population difference is stronger than that of the band velocity and the derivative of electron population difference with the time.

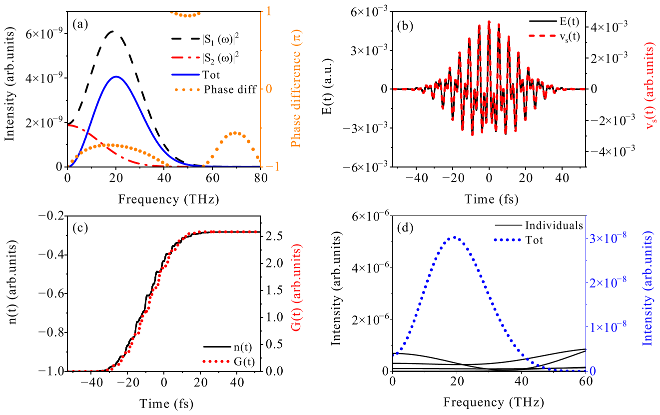

FIG. 4. Same as Fig. 3, but the pulse duration of two-color laser is 106 fs.

We then construct the interference model to analyze the THz emissions. Since $\mathbf{v}_c(t)$ in $S_1(t)$ is related to energy band and laser pulse, results near the Dirac cone contribute mostly to the THz radiation (below 100 THz). We can ignore the region far away from the Dirac point $|\mathbf{k}-\mathbf{k}_D| > 0.2$ a.u. and define that $\mathbf{v}_s(t) = \int_{BZ}\frac{d\mathbf{v}_c(t)}{dt}d\mathbf{k}$ and $\mathbf{v}_s(t)$ can be simplified as $v_s(t)$ when ignoring laser pulses in the $y$-polarized direction. $v_s(t)$ versus time are plotted in Figs. 3(b), 4(b), and 5(b). For comparison, laser pulses $E(t)$ are also plotted in these figures. One can see that $v_s(t)$ induced by electrons near Dirac cones is consistent with $E(t)$, differing only by a constant. Therefore, in the interference model, we use $E(t)$ to replace $v_s(t)$ (or $\int_{BZ}\frac{d\mathbf{v}_c(t)}{dt}d\mathbf{k}$ in the $x$-polarized direction).

In addition, population difference $n(t) = \int_{BZ} n^{\mathbf{k}}(t)d\mathbf{k}$ is one of the important factors for determining the THz emission, which can be related to Landau- Zener tunneling rate. Considering the influence of electron motions near Dirac cone, Landau-Zener tunneling rate $P_{\mathbf{k}}(t)$ can be explicitly

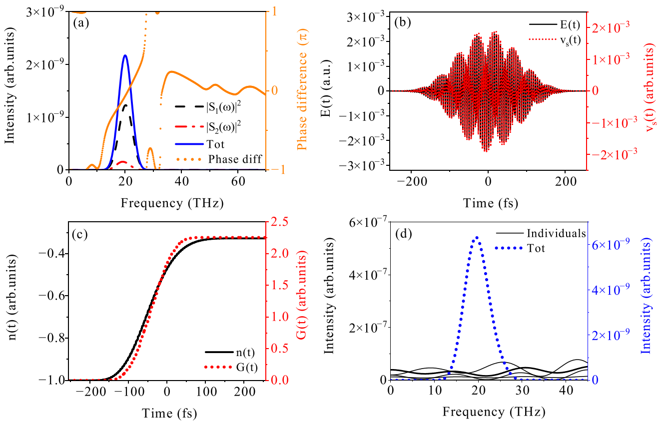

FIG. 5. Same figure as Fig. 3 except for the pulse duration of two-color laser of 512 fs.

expressed as

$$P_{\mathbf{k}}(t) = \exp\left[\frac{-\pi\Delta^2/\hbar}{|2v_F\cos(\theta_{\mathbf{k}})E_p(t)|}\right], \tag{17}$$

where $v_F$ is Fermi velocity, $\theta_{\mathbf{k}}$ is directional angle, and $\Delta$ is energy difference near Dirac cone. Note that the energy difference $\Delta$ is defined under the Bloch basis, which is the same quantity as the energy gap $E_g$ mentioned in Sec. II A in the electron-hole picture. According to Dirac-Fermi distributions, the probabilities are added up near the Dirac cone, in which $|\mathbf{k} - \mathbf{k}_D| < 0.2$ a.u. with $\mathbf{k}_D$ as the position of Dirac cone. We then obtain

$$P_\sigma(t) = \int P_{\mathbf{k}}(t)d\mathbf{k}. \tag{18}$$

To compare with the variation of $n(t)$ with time, we introduce

$$G(t) = \int_{-\infty}^{t} P_\sigma(t)dt. \tag{19}$$

We show results of $n(t)$ and $G(t)$ in Figs. 3(c), 4(c), and 5(c). The comparison indicates that with the time, the function $G(t)$ related to Landau-Zener tunneling rate near the Dirac cone is in complete accord with population difference $n(t)$. Thus, in the interference model, we use $G(t)$ to replace $n(t)$.

In our interference model, the time of laser pulse lasting is divided as a number of equal time interval, which is five optical cycles of 800-nm laser, we use $G(t)$ and $E(t)$ to calculate the intraband current in Eq. (15) for individual interval. The Fourier transform of the current (or THz emission) is plotted in Figs. 3(d), 4(d), and 5(d). Each black line means the THz emissions from a time interval. With the increase of laser duration, the number of black lines is increased. THz emissions from each time interval are relatively weak. After interference of many time intervals, the THz emissions become stronger and stronger. Meanwhile the intercycle interference lead to more and more narrower width of THz emissions with the increase of laser duration. And the spectral shapes of 20-THz emissions are precisely reproduced for three laser durations, which can be well compared with those in Fig. 1.

### 2. *Four-wave mixing model*

We next employ the four-wave mixing model to analyze the THz emissions by long duration of 512 fs. Since the fundamental wavelength is 800 nm in the two-color combination, this model can predict the second wavelength for a given THz frequency. This frequency fulfills Stokes peaks $|2\omega_1 - \omega_2|$ and anti-Stokes peaks $|2\omega_2 - \omega_1|$. Considering four cases (i) $\lambda_2 < \lambda_1$ and $2\lambda_2 > \lambda_1$, (ii) $\lambda_2 < \lambda_1$ and $2\lambda_2 < \lambda_1$, (iii) $\lambda_2 > \lambda_1$ and $2\lambda_1 > \lambda_2$, and (iv) $\lambda_2 > \lambda_1$ and $2\lambda_1 < \lambda_2$, there exist Stokes peak $2\omega_1 - \omega_2$, Stokes peak $\omega_2 - 2\omega_1$, anti-Stokes peak $2\omega_2 - \omega_1$, and anti-Stokes peak $\omega_1 - 2\omega_2$. Thus, for a frequency of 10 THz, $\lambda_2$ can be derived as 395.08 nm, 405.76 nm, 1558.81 nm, and 1645.27 nm, $\lambda_2$ are 389.95 nm, 411.32 nm, 1520.31 nm, and 1691.61 nm for 20 THz, and they are 384.95 nm, 417.03 nm, 1482.78 nm, and 1740.61 nm for 30 THz. We set the intensity ratio of the fundamental to the second color as 1, and calculate the THz emissions by solving the SBE equations in Sec. II. The simulated THz spectra are shown in Fig. 6 for three different THz frequencies. For each THz frequency, two long wavelengths of $\lambda_2$ result two strong THz peaks while two short wavelengths give two weak peaks. At different THz frequencies, shapes (or widths) of THz spectra are about the same for four wavelengths of $\lambda_2$. Then we take an example of the second wavelength at anti-Stokes peak $\omega_1 - 2\omega_2$, and plot the THz yields versus relative phase $\phi_2$ in Fig. 6(d). At different THz frequencies, THz yields are not sensitive to $\phi_2$ at all.

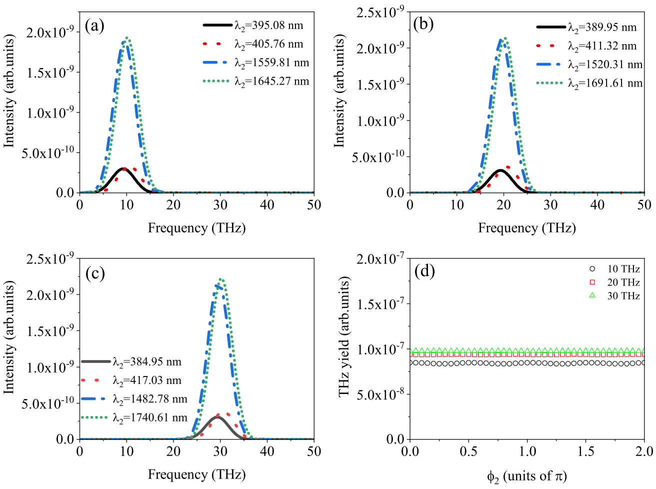

FIG. 6. THz emissions calculated by using estimated $\lambda_2$ from four-wave mixing model at central frequencies of (a) 10 THz, (b) 20 THz, and (c) 30 THz. Pulse duration of two-color laser is 512 fs. Intensity of fundamental color is assumed the same as that of second color. (d) Integrated THz yields versus relative phase $\phi_2$ for different THz spectral regions.

From Fig. 6, we find that $\lambda_2$ at anti-Stokes peak $\omega_1 - 2\omega_2$ is the best for generating THz yields, which also agrees with the optimal wavelength obtained by GA in Table I. This can be explained by $G(t)$ in Eq. (19), which is closely related to the population difference $n(t)$. From Eq. (17), the Landau-Zener tunneling rate $P_{\mathbf{k}}(t) \propto |E(t)|$ and $P_{\mathbf{k}}(t) \propto 1/\Delta$, thus leading to $G(t) \propto \int_{-\infty}^{t} |E(t)|dt$ and $G(t) \propto 1/\Delta$. For optimal generation of THz emissions, $\int_{-\infty}^{+\infty} |E(t)|^2 dt$ is always maximized, which does not depend on the optimal parameters. In other words, $\int_{-\infty}^{+\infty} |E(t)|^2 dt = C$. From Eq. (19), we can obtain

$$G(t) \propto \int_{-\infty}^{t} |E_{01}(t) + E_{02}(t)|dt. \tag{20}$$

Since $\phi_2$ plays no role in the THz emission, we can get

$$G(t) \propto |A_{01}(t)| + |A_{02}(t)|, \tag{21}$$

where $A_{01}(t) = \int_{-\infty}^{t} E_{01}(t)dt$ and $A_{02}(t) = \int_{-\infty}^{t} E_{02}(t)dt$. Then we consider results near the peak of two-color laser pulse,

$$|G(t)|_{\max} \propto \frac{E_1}{\omega_1} + \frac{E_2}{\omega_2}. \tag{22}$$

It is known that $E_1 \approx E_2$ and $\lambda_1 = 800$ nm. We have $|G(t)|_{\max} \propto \frac{1}{\omega_2}$, meaning that the longest wavelength results in the biggest $|G(t)|_{\max}$. Thus among four possible wavelengths predicted by the four-wave mixing model, the longest one

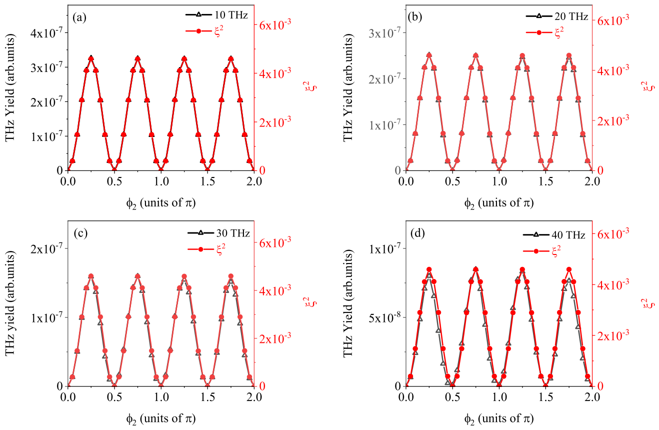

FIG. 7. Variation of integrated THz yields (black lines) and asymmetry parameter (red lines) with relative phase $\phi_2$ at central frequencies of (a) 10 THz, (b) 20 THz, (c) 30 THz, and (d) 40 THz. Simulation parameters are taken from Table III except for $\phi_2$. Pulse duration of two-color laser is 53 fs.

at anti-Stokes peak $\omega_1 - 2\omega_2$ leads to the strongest THz emissions.

### 3. *Asymmetric parameter model*

We next apply the asymmetric parameter model to analyze the THz emissions with the relative phase by short duration of 53 fs. In this model, the asymmetry parameter $\xi$ can be written as [46]

$$\xi = P_-(t_\infty) - P_+(t_\infty),$$
$$P_-(t_\infty) = \int_{-\infty}^{0}\int_{-\infty}^{-\infty}[\rho_{cc}(t_\infty) - \rho_{vv}(t_\infty)]dk_y dk_x,$$
$$P_+(t_\infty) = \int_{0}^{+\infty}\int_{-\infty}^{-\infty}[\rho_{cc}(t_\infty) - \rho_{vv}(t_\infty)]dk_y dk_x. \quad (23)$$

This parameter can well reflect the electron population difference between conduction and valence bands, which has been used to analyze the laser-induced current in solids [70]. We use the optimized parameters except for relative phase $\phi_2$ in Table III obtained at 10, 20, 30, and 40 THz, and calculate the THz spectra. The integrated THz yields (black lines) as a function of the relative phase $\phi_2$ are plotted in Figs. 7(a)–7(d). For comparison, in each figure, the square of asymmetry parameter $\xi^2$ (red line) is also present, and is normalized with the integrated THz yields at $\phi_2 = 0.25\pi$. It shows that the asymmetry parameter can well reproduce the dependence of THz emission yields on the relative phase for 10, 20, and 30 THz, and some deviations occur for 40 THz. This indicates that the generation of low-frequency THz emissions (10–30 THz) is mainly determined by the symmetry of laser-graphene system, which can be well described by the asymmetry parameter, while for high-frequency THz generation, the nonlinear properties of material [58] also become important, which is not included in the asymmetry parameter.

Although the influence of laser duration on the THz emission has been studied in hydrogen and nitrogen targets [71], the change of physical mechanism and the variation of THz spectral width with the laser duration have not been addressed. Thus we can conclude that the THz emission is due to the interplay of the symmetry of laser pulse and the four-wave mixing, which is much dependent on the pulse duration of driving two-color laser. When the symmetry of laser pulse becomes dominant, the optimal relative phase from our work is consistent with that in Refs. [16,72]. At the optimal relative phase, both low and high THz yields can be simultaneously enhanced since the THz spectrum has a broadband. This is usually true for two-color laser pulses with the short pulse duration. Furthermore, the generation mechanism of THz emission is also dependent on the intensity ratio between the fundamental and the second color. When the symmetry of laser pulse plays a major role, the intensity ratio is smaller, which agrees with Thiele *et al.*'s [72]. And the intensity ratio becomes much larger if the four-wave mixing is dominant.

TABLE IV. Optimized laser parameters for generating THz emissions at a central frequency of 20 THz from gapped graphene. Results are listed for different initial random numbers (idum) in the GA. Energy gap $\Delta = 3$ eV. Pulse duration of two-color laser is 512 fs.

| idum | $\lvert E_1\rvert^2$ | $\lvert E_2\rvert^2$ | $\lambda_2$ (nm) | $\phi_2$ ($\pi$) |
|---|---|---|---|---|
| 1 | 0.0888 | 0.1087 | 1690.6 | 0.101 |
| 2 | 0.0889 | 0.1086 | 1690.7 | 0.456 |
| 3 | 0.0890 | 0.1085 | 1690.9 | 0.103 |
| 4 | 0.0884 | 0.1091 | 1690.5 | 0.144 |
| 5 | 0.0886 | 0.1089 | 1690.4 | 0.121 |

## C. Optimized laser parameters for generating tunable THz emissions from doped graphene

In general, energy gap leads to difference in the longitudinal current from single-layer graphene. We then run the GA program, and check how the optimal laser parameters are modified for gapped (or doped) graphene. In the optimization, we set band gap $\Delta = 3$ eV, ignore the transition dipole phase, and maintain the damage fluence threshold below 150 mJ/cm$^2$. The optimized parameters include the fundamental intensity $|E_1|^2$, second-color intensity $|E_2|^2$, wavelength of second color $\lambda_2$, and relative phase $\phi_2$. For a given frequency of 20 THz, the optimized laser parameters are listed in Tables IV–VI for laser durations of 512 fs, 106 fs, and 53 fs, respectively. Results are obtained by starting from different random numbers (distinguished by using "idum" in the table) for each case. Optimal $\lambda_2$, $|E_1|^2$, and $|E_2|^2$ are very

TABLE V. Same as Table IV, but pulse duration of two-color laser is 106 fs.

| idum | $\lvert E_1\rvert^2$ | $\lvert E_2\rvert^2$ | $\lambda_2$ (nm) | $\phi_2$ ($\pi$) |
|---|---|---|---|---|
| 1 | 0.4140 | 0.5340 | 1678.3 | 0.006 |
| 2 | 0.4142 | 0.5338 | 1678.2 | 1.002 |
| 3 | 0.4139 | 0.5341 | 1678.1 | 0.997 |
| 4 | 0.4136 | 0.5344 | 1678.6 | 0.980 |
| 5 | 0.4135 | 0.5345 | 1677.7 | 0.985 |

TABLE VI. Same table as Table IV except for two-color pulse duration of 53 fs.

| idum | $\|E_1\|^2$ | $\|E_2\|^2$ | $\lambda_2$ (nm) | $\phi_2$ ($\pi$) |
|---|---|---|---|---|
| 1 | 0.954 | 1.416 | 1602.3 | 0.249 |
| 2 | 0.955 | 1.415 | 1601.6 | 0.249 |
| 3 | 0.958 | 1.412 | 1601.3 | 1.249 |
| 4 | 0.947 | 1.423 | 1603.3 | 0.749 |
| 5 | 0.954 | 1.416 | 1601.3 | 0.249 |

stable in each table and they are about the same as those at 20 THz in Tables I–III. While the relative phase is varied with the random number for fixed laser duration, and its change law is consistent with what we have identified for zero-gap graphene. We have also set $\Delta = 5$ eV and found that optimal laser parameters remain unchanged (not shown). So one can conclude that energy gap $\Delta$ does not alter the optimal parameters in the two-color laser pulses for maximizing the THz emissions.

We show the THz spectra from single-layer graphene with different energy gaps in Fig. 8. Under optimal laser parameters, THz emissions are gradually decreased with the increase of energy gap $\Delta$. Since THz emissions in 0–100 THz frequency band are mainly determined by the intraband current near Dirac cone, while harmonics in higher-frequency regions are mostly due to the interband current far from Dirac cone [57]. We thus explain the change of THz emissions by referring to Landau-Zener tunneling rate near Dirac cone, which is related to the absolute value of transition dipole moment, the laser intensity, and the energy gap. The absolute value of transition dipole moment can be written as

$$|D_{cv}(\mathbf{k})| \propto \frac{|P_{cv}(\mathbf{k})|}{[E_c(\mathbf{k}) - E_v(\mathbf{k})]}, \tag{24}$$

where $P_{cv}(\mathbf{k})$ is $\langle\phi_c(\mathbf{k})|\hat{p}|\phi_v(\mathbf{k})\rangle$, $\phi_s(\mathbf{k})$ is the normalized wave function of each $\mathbf{k}$ point in a given band, $E_c(\mathbf{k})$ and $E_v(\mathbf{k})$ are band energy in valence band and conduction band, respectively. Since $|D_{cv}(\mathbf{k})| = |2v_F\cos(\theta_{\mathbf{k}})/\Delta|$, Eq. (17) can be rewritten as

$$P_{\mathbf{k}}(t) \propto \exp\left[\frac{-\pi\Delta/\hbar}{|D_{cv}(\mathbf{k})E_p(t)|}\right]. \tag{25}$$

For different energy gaps, optimized laser parameters are about the same, so the maximum intensity near laser peak is remaining the same. Landau-Zener tunneling probability $|P_{\mathbf{k}}(t)|_{\max}$ near laser peak is mostly determined by $|D_{cv}(\mathbf{k})|$ and energy gap $\Delta$. Transition dipole moment $|D_{cv}(\mathbf{k})|$ decreases with the increase of $\Delta$. Therefore, larger energy gap leads to smaller $|P_{\mathbf{k}}(t)|_{\max}$ from Eq. (25), so does the THz emission in Fig. 8.

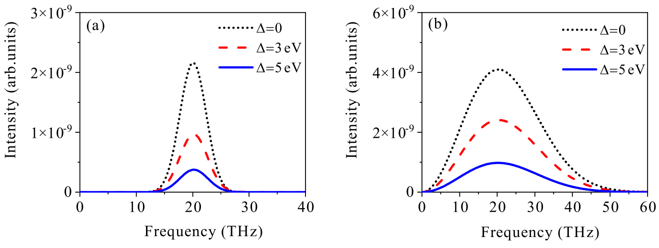

FIG. 8. Simulated THz emissions obtained with different energy gaps $\Delta$ for two-color laser durations of (a) 512 fs and (b) 106 fs.

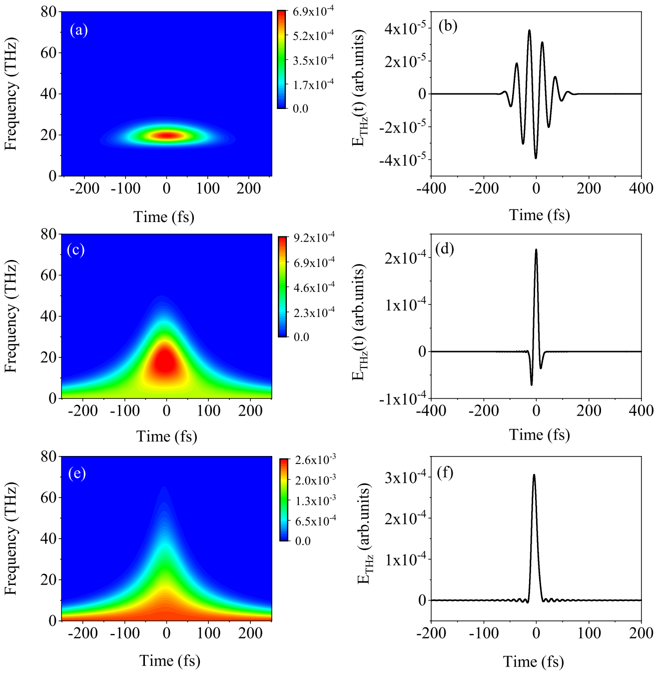

FIG. 9. Time-frequency analysis of THz emissions [(a), (c), and (e)] and temporal waveforms by synthesizing THz emissions in a bandwidth of 0–100 THz [(b), (d), and (f)]. Central frequency is fixed at 20 THz. First row: two-color laser duration of 512 fs; second row: 106 fs; and third row: 53 fs.

### D. Temporal THz waveforms by optimized two-color laser pulses

Finally, we check the temporal characteristics of THz emissions. We show the time-frequency pictures of THz emissions with the central frequency of 20 THz in Fig. 9. The temporal THz waveforms are also plotted when THz emissions are synthesized in a spectral range of 0–100 THz. For the long pump laser (512 fs), THz emissions are concentrated around 20 THz (in frequency) and around the peak of laser pulse (in time), see Fig. 9(a), and the temporal synthesized THz waveform presents the few-cycle structure, see Fig. 9(b). When the pulse width of driving laser is decreased to 106 fs, THz emissions in Fig. 9(c) become much broader in frequency covering a more extensive THz range, and near single-cycle pulse can be obtained in Fig. 9(d). For the shortest duration (53 fs), THz emissions are further extended both in frequency and in time, as shown in Fig. 9(e), and one can get a half-cycle synthesized THz waveform in Fig. 9(f). Note that long emission times in Figs. 9(c) and 9(e) indicate that there are weak direct current contributing to the THz waves, and THz emissions are originated from asymmetry of laser-graphene system.

We also examine the variation of THz waves obtained by optimized two-color laser pulses with duration of 512 fs. Figure 10(a) shows THz spectra at 20 THz by varying the relative

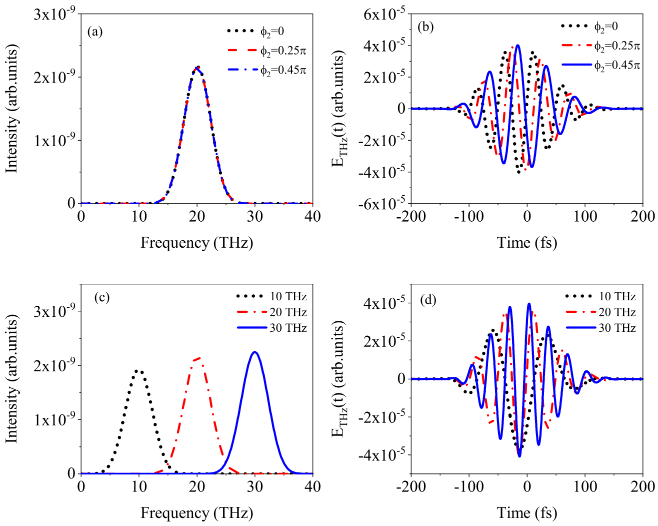

FIG. 10. Temporal THz waveforms generated by optimal two-color laser pulses with duration of 512 fs. (a) THz spectra at 20 THz for three relative phases and (b) corresponding waveforms by synthesizing THz emissions with a bandwidth of 0–100 THz. (c) THz spectra at different central frequencies and (d) resulted few-cycle waveforms.

phase $\phi_2$. The THz spectral intensity does not change with the relative phase. Synthesized THz waveforms in Fig. 10(b) show the change of their carrier envelope phases (CEPs). This indicates that the CEP of THz wave can be tuned by the relative phase in the two-color long laser pulse. Figures 10(c) and 10(d) show THz spectra at different central frequencies and THz waveforms by synthesizing different THz emissions in a fixed bandwidth of 0–100 THz. Different few-cycle THz waveforms can be obtained by changing the central THz frequency. This means that THz waveforms can be tunable by changing optimal laser parameters in the two-color synthesis. In general, THz waves from single-layer graphene can be tuned efficiently by changing two-color laser parameters, which could be useful for nonlinear THz spectroscopy, wireless communications, and so forth.

## IV. CONCLUSIONS

In summary, we showed that central-frequency tunable THz emissions can be optimally generated at normal incidence from single-layer graphene by using two-color laser pulses with different durations. We employed the genetic algorithm (GA) to obtain the optimized laser parameters in the two-color combination, consisting of an 800-nm laser and a longer-wavelength one, which is different from the traditional scheme of the 800-nm laser and its second-harmonic field [16]. We found that optimal parameters show quite different behaviors for different two-color durations. For long pump laser (512 fs), optimal THz emissions are mainly determined by two laser frequencies while phase difference and intensity ratio play a secondary role. For medium-width field (106 fs), THz emissions depend on both the relative phase and the wavelength of second-color laser. For two-color laser with short duration (53 fs), THz emissions are very sensitive to the relative phase between two colors, meaning that subcycle waveforms are crucial for THz generation. We applied three models to interpret the generation of THz emissions. We established an interference model from the photoelectron current model, and revealed that intercycle interference of electron current determines the spectral shape and width of THz spectra driven by two-color pulses with different durations. We adopted the four-wave mixing model to obtain the wavelengths of second color for long-duration pulse, and explained that the wavelength satisfies with anti-Stokes peak can generate the optimal THz emissions in terms of Landau-Zener tunneling rate. We also introduced an asymmetry parameter to mimic the change of THz yields with relative phase between two colors when the driving laser pulse has a short duration. In addition, we optimized the two-color laser parameters for maximizing the THz emissions from gapped graphene by using the GA. It shows that optimal parameters do not depend on the energy gap, and resulted THz yields are decreased with the energy gap. Finally, we examined time-frequency pictures of THz emissions and synthesized THz waveforms, and showed that CEP-adjusted THz waves or frequency-controlled THz waves can be feasibly generated by selecting optimized laser parameters under the two-color scheme.

With advancement in optical parametric amplification and optical parametric chirped-pulse amplification technology, nowadays, it is possible to generate nearly arbitrary optical waves by synthesizing multicolor laser pulse in experiment [73–76]. We expect that it will be promising to generate the waveform-controlled THz waves for wide applications by applying the technique of multicolor laser synthesis into solid targets.

## ACKNOWLEDGMENTS

This work was supported by National Natural Science Foundation of China (NSFC) under Grants No. 12274230, No. 12204238, No. 11964033, and No. 11834004, Funding of Nanjing University of Science and Technology (NJUST) under Grant No. TSXK2022D005, and Natural Science Foundation of Jiangsu Province under Grant No. BK20220925.

[1] B. Ferguson and X. C. Zhang, Nature Mater. **1**, 26 (2002).

[2] A. Dobroiu, C. Otani, and K. Kawase, Meas. Sci. Technol. **17**, R161 (2006).

[3] H. Y. Hwang, S. Fleischer, N. C. Brandt, B. G. Perkins, Jr., M. Liu, K. Fan, A. Sternbach, X. Zhang, R. D. Averitt, and K. A. Nelson, J. Mod. Opt. **62**, 1447 (2015).

[4] Y. Huang, C. Meng, X. Wang, Z. Lü, D. Zhang, W. Chen, J. Zhao, J. Yuan, and Z. Zhao, Phys. Rev. Lett. **115**, 123002 (2015).

[5] T. Nagatsuma, G. Ducournau, and C. C. Renaud, Nature Photon. **10**, 371 (2016).

[6] R. M. Woodward, V. P. Wallace, D. D. Arnone, E. H. Linfield, and M. Pepper, J. Biol. Phys. **29**, 257 (2003).

[7] K. Reimann, Rep. Prog. Phys. **70**, 1597 (2007).

[8] H. Hamster, A. Sullivan, S. Gordon, W. White, and R. W. Falcone, Phys. Rev. Lett. **71**, 2725 (1993).

[9] Q. Jin, K. Williams, E. Y. Wen, J. Dai, and X.-C. Zhang, Appl. Phys. Lett. **111**, 071103 (2017).

[10] Y. E, L. Zhang, A. Tcypkin, S. Kozlov, C. Zhang, and X.-C. Zhang, Ultrafast Sci. **2021**, 9892763 (2021).

[11] J. Déchard, X. Davoine, and L. Bergé, Phys. Rev. Lett. **123**, 264801 (2019).

[12] A. Sagisaka, H. Daido, S. Nashima, S. Orimo, K. Ogura, M. Mori, A. Yogo, Jinglong Ma, I. Daito, A. Pirozhkov, S. Bulanov, T. Esirkepov, K. Shimizu, and M. Hosoda, Appl. Phys. B **90**, 373 (2008).

[13] C. Hauri, C. Ruchert, C. Vicario, and F. Ardana, Appl. Phys. Lett. **99**, 161116 (2011).

[14] J. H. Jeong, B. Kang, J. S. Kim, M. Jazbinsek, S. H. Lee, S. C. Lee, I. Baek, H. Yun, J. Kim, Y. Lee, J. H. Lee, J. H. Kim, F. Rotermund, and O. Kwon, Sci. Rep. **3**, 3200 (2013).

[15] H. Hafez, S. Kovalev, J. Deinert, Z. Mics, B. Green, N. Awari, M. Chen, S. Germanskiy, U. Lehnert, J. Teichert, Z. Wang, K.-J. Tielrooij, Z. Liu, Z. Chen, A. Narita, K. Müllen, M. Bonn, M. Gensch, and D. Turchinovich, Nature (London) **561**, 507 (2018).

[16] K. Y. Kim, J. H. Glownia, A. J. Taylor, and G. Rodriguez, Opt. Express **15**, 4577 (2007).

[17] I. Babushkin, S. Skupin, A. Husakou, C. Köhler, E. Cabrera-Granado, L. Bergé, and J. Herrmann, New J. Phys. **13**, 123029 (2011).

[18] A. Debayle, L. Gremillet, L. Bergé, and C. Köhler, Opt. Express **22**, 13691 (2014).

[19] K. Zhang, Y. Zhang, X. Wang, T.-M. Yan, and Y. H. Jiang, Photon. Res. **8**, 760 (2020).

[20] X. Xie, J. Dai, and X.-C. Zhang, Phys. Rev. Lett. **96**, 075005 (2006).

[21] N. Karpowicz and X. C. Zhang, Phys. Rev. Lett. **102**, 093001 (2009).

[22] Z. Zhou, D. Zhang, Z. Zhao, and J. Yuan, Phys. Rev. A **79**, 063413 (2009).

[23] Z. Zhou, Z. Lv, D. Zhang, Z. Zhao, and C. D. Lin, Phys. Rev. A **101**, 043422 (2020).

[24] M. Kress, T. Löffler, S. Eden, M. Thomson, and H. G. Rokos, Opt. Lett. **29**, 1120 (2004).

[25] T. Bartel, K. Reimann, M. Woerner, and T. Elsaeeer, Opt. Lett. **30**, 2805 (2005).

[26] V. A. Andreeva, O. G. Kosareva, N. A. Panov, D. E. Shipilo, P. M. Solyankin, M. N. Esaulkov, P. González de Alaiza Martínez, A. P. Shkurinov, V. A. Makarov, L. Bergé, and S. L. Chin, Phys. Rev. Lett. **116**, 063902 (2016).

[27] L. L. Zhang, W. M. Wang, T. Wu, R. Zhang, S. J. Zhang, C. L. Zhang, Y. Zhang, Z. M. Sheng, and X. C. Zhang, Phys. Rev. Lett. **119**, 235001 (2017).

[28] D. J. Cook and R. M. Hochstrasser, Opt. Lett. **25**, 1210 (2000).

[29] S.-W. Huang, G. Cirmi, J. Moses, K.-H. Hong, S. Bhardwaj, J. R. Birge, L.-J. Chen, E. Li, B. J. Eggleton, G. Cerullo, and F. X. Kärtner, Nature Photon. **5**, 475 (2011).

[30] D. Greening, B. Weaver, A. J. Pettipher, D. Walke, E. Larsen, J. Marangos, and J. Tisch, Opt. Express **28**, 23329 (2020).

[31] E. Takahashi, P. Lan, O. Mücke, Y. Nabekawa, and K. Midorikawa, Nature Commun. **4**, 2691 (2013).

[32] C. Jin and C. D. Lin, Chin. Phys. B **25**, 094213 (2016).

[33] L. He, G. Yuan, K. Wang, W. Hua, C. Yu, and C. Jin, Photon. Res. **7**, 1407 (2019).

[34] I. J. Kim, C. M. Kim, H. T. Kim, G. H. Lee, Y. S. Lee, J. Y. Park, D. J. Cho, and C. H. Nam, Phys. Rev. Lett. **94**, 243901 (2005).

[35] H. Du, H. Wang, and B. Hu, Phys. Rev. A **81**, 063813 (2010).

[36] P. Lan, E. J. Takahashi, and K. Midorikawa, Phys. Rev. A **82**, 053413 (2010).

[37] J. G. Chen, S. L. Zeng, and Y. J. Yang, Phys. Rev. A **82**, 043401 (2010).

[38] Z. Zeng, Y. Cheng, X. Song, R. Li, and Z. Xu, Phys. Rev. Lett. **98**, 203901 (2007).

[39] C. Jin, G. Wang, H. Wei, A. T. Le, and C. D. Lin, Nature Commun. **5**, 4003 (2014).

[40] C. Jin and C. D. Lin, Photon. Res. **6**, 434 (2018).

[41] G. Vampa, T. J. Hammond, N. Thire, B. E. Schmidt, F. Legare, C. R. McDonald, T. Brabec, and P. B. Corkum, Nature (London) **522**, 462 (2015).

[42] J. B. Li, Xiao Zhang, S. J Yue, H. M. Wu, B. T. Hu, and H. C. Du, Opt. Express **25**, 18603 (2017).

[43] X. H. Song, S. D. Yang, R. X. Zuo, T. Meier, and W. F. Yang, Phys. Rev. A **101**, 033410 (2020).

[44] H. K. Avetissian, G. F. Mkrtchian, and A. Knorr, Phys. Rev. B **105**, 195405 (2022).

[45] Q. F. Peng, Z. Y. Peng, Y. Lang, Y. L. Zhu, D. W. Zhang, Z. H. Lü, and Z. X. Zhao, Chin. Phys. Lett. **39**, 053301 (2022).

[46] Z. Guan, B. Wang, G.-L. Wang, X.-X. Zhou, and C. Jin, Opt. Express **30**, 26912 (2022).

[47] D. Zhang, Z. Lü, C. Meng, X. Du, Z. Zhou, Z. Zhao, and J. Yuan, Phys. Rev. Lett. **109**, 243002 (2012).

[48] L. Zhang, G. L. Wang, S. F. Zhao, and X. X. Zhou, Phys. Plasmas **24**, 023116 (2017).

[49] S. Jiang, H. Wei, J. Chen, C. Yu, R. Lu, and C. D. Lin, Phys. Rev. A **96**, 053850 (2017).

[50] M. S. Mrudul and G. Dixit, Phys. Rev. B **103**, 094308 (2021).

[51] C. Liu, Y. Zheng, Z. Zeng, and R. Li, Phys. Rev. A **97**, 063412 (2018).

[52] A. H. Castro Neto, F. Guinea, N. M. R. Peres, K. S. Novoselov, and A. K. Geim, Rev. Mod. Phys. **81**, 109 (2009).

[53] D. Sun, G. Aivazian, A. M. Jones, J. S. Ross, W. Yao, D. Cobden, and X. D. Xu, Nature Nanotech **7**, 114 (2012).

[54] F. J. G. de Abajo, ACS Photonics **1**, 135 (2014).

[55] Z. M. Sheng, K. Mima, J. Zhang, and H. Sanuki, Phys. Rev. Lett. **94**, 095003 (2005).

[56] G. Q. Liao, Y. T. Li, Y. H. Zhang, H. Liu, X. L. Ge, S. Yang, W. Q. Wei, X. H. Yuan, Y. Q. Deng, B. J. Zhu, Z. Zhang, W. M. Wang, Z. M. Sheng, L. M. Chen, X. Lu, J. L. Ma, X. Wang, and J. Zhang, Phys. Rev. Lett. **116**, 205003 (2016).

[57] B. Sensale-Rodriguez, R. Yan, M. M. Kelly, T. Fang, K. Tahy, W. S. Hwang, D. Jena, L. Liu, and H. G. Xing, Nature Commun. **3**, 780 (2012).

[58] J. Maysonnave, S. Huppert, F. Wang, S. Maero, C. Berger, W. de Heer, T. B. Norris, L. A. De Vaulchier, S. Dhillon,

J. Tignon, R. Ferreira, and J. Mangeney, Nano Lett. **14**, 5797 (2014).

[59] I. Al-Naib, J. E. Sipe, and M. M. Dignam, Phys. Rev. B **90**, 245423 (2014).

[60] I. Al-Naib, M. Poschmann, and M. M. Dignam, Phys. Rev. B **91**, 205407 (2015).

[61] L. P. Zhu, Z. H. Yao, Y. Y. Huang, C. He, B. G. Quan, J. J. Li, C. Z. Gu, X. L. Xu, and Z. Y. Ren, Phys. Rev. Appl. **12**, 044063 (2019).

[62] P. Navaeipour and M. M. Dignam, Phys. Rev. B **105**, 115431 (2022).

[63] Z. Guan, G. L. Wang, L. Zhang, Z. H. Jiao, S. F. Zhao, and X. X. Zhou, Chin. Phys. Lett. **38**, 054201 (2021).

[64] C. Heide, Tobias Boolakee, T. Eckstein, and P. Hommelhoff, Nanophoto **10**, 3701 (2021).

[65] T. Higuchi, C. Heide, K. Ullmann, H. B. Weber, and P. Hommelhoff, Nature (London) **550**, 224 (2017).

[66] T. Tamaya, A. Ishikawa, T. Ogawa, and K. Tanaka, Phys. Rev. B **94**, 241107(R) (2016).

[67] T. Tamaya, A. Ishikawa, T. Ogawa, and K. Tanaka, Phys. Rev. Lett. **116**, 016601 (2016).

[68] F. L. Dong, Q. Z. Xia, and J. Liu, Phys. Rev. A **104**, 033119 (2021).

[69] K. L. Ishikawa, New J. Phys. **15**, 055021 (2013).

[70] E. Wu, C. J. Zhang, Z. S. Wang, and C. P. Liu, New J. Phys. **22**, 033016 (2020).

[71] W. M. Wang, P. Gibbon, Z. M. Sheng, and Y. T. Li, Phys. Rev. A **90**, 023808 (2014).

[72] I. Thiele, P. González de Alaiza Martínez, R. Nuter, A. Nguyen, L. Bergé, and S. Skupin, Phys. Rev. A **96**, 053814 (2017).

[73] A. Wirth, M. T. Hassan, I. Grguraš, J. Gagnon, A. Moulet, T. T. Luu, S. Pabst, R. Santra, Z. A. Alahmed, A. M. Azzeer, V. S. Yakovlev, V. Pervak, F. Krausz, and E. Goulielmakis, Science **334**, 195 (2011).

[74] P. Wei, J. Miao, Z. Zeng, C. Li, X. Ge, R. Li, and Z. Xu, Phys. Rev. Lett. **110**, 233903 (2013).

[75] S. Haessler, T. Balčiunas, G. Fan, G. Andriukaitis, A. Pugžlys, A. Baltuška, T. Witting, R. Squibb, A. Zaïr, J. W. G. Tisch, J. P. Marangos, and L. E. Chipperfield, Phys. Rev. X **4**, 021028 (2014).

[76] B. Xue, Y. Tamaru, Y. X. Fu, H. Yuan, P. Lan, O. Mücke, A. Suda, K. Midorikawa, and E. Takahashi, Ultrafast Sci. **2021**, 9828026 (2021).